

Graphene-deposited photonic crystal fibers for continuous refractive index sensing applications

Y. C. Tan,¹ Z. Q. Tou,² K. K. Chow,^{1,*} and C. C. Chan²

¹ School of Electrical and Electronic Engineering,
Nanyang Technological University, 50 Nanyang Avenue, Singapore 639798

² School of Chemical and Biomedical Engineering,
Nanyang Technological University, 70 Nanyang Drive, Singapore 637457
*kkchow@ntu.edu.sg

Abstract: We present a pilot demonstration of an optical fiber based refractive index (RI) sensor involving the deposition of graphene onto the surface of a segment of a photonic crystal fiber (PCF) in a fiber-based Mach-Zehnder Interferometer (MZI). The fabrication process is relatively simple and only involves the fusion splicing of a PCF between two single mode fibers. The deposition process relies only on the cold transfer of graphene onto the PCF segment, without the need for further physical or chemical treatment. The graphene overlay modified the sensing scheme of the MZI RI sensor, allowing the sensor to overcome limitations to its detectable RI range due to free spectral range issues. This modification also allows for continuous measurements to be obtained without the need for reference values for the range of RIs studied and brings to light the potential for simultaneous dual parameter sensing. The sensor was able to achieve a RI sensitivity of 9.4 dB/RIU for the RIs of 1.33-1.38 and a sensitivity of 17.5 dB/RIU for the RIs of 1.38-1.43. It also displayed good repeatability and the results obtained were consistent with the modeling.

OCIS codes: (060.2370) Fiber optic sensors; (160.4236) Nanomaterials.

References and links

1. R. Jha, J. Villatoro, and G. Badenes, "Ultraprecise reflection photonic crystal fiber modal interferometer for accurate refractive index sensing," *Appl. Phys. Lett.* **93**, 191106 (2008).
2. R. Jha, J. Villatoro, G. Badenes, and V. Pruneri, "Refractometry based on a photonic crystal fiber interferometer," *Opt. Lett.* **34**, 617-619 (2009).
3. K. S. Park, H. Y. Choi, S. J. Park, U.-C. Paek, and B. H. Lee, "Temperature robust refractive index sensor based on a photonic crystal fiber interferometer," *IEEE Sensors J.* **10**, 1147-1148 (2010).
4. W. C. Wong, C. C. Chan, L. H. Chen, Z. Q. Tou, and K. C. Leong, "Highly sensitive miniature photonic crystal fiber refractive index sensor based on mode field excitation," *Opt. Lett.* **36**, 1731-1733 (2011).
5. M. Deng, C. P. Tang, T. Zhu, and Y. J. Rao, "Highly sensitive bend sensor based on Mach-Zehnder interferometer using photonic crystal fiber," *Opt. Commun.* **284**, 2849-2853 (2011).
6. W. J. Zhou, W. C. Wong, C. C. Chan, L. Y. Shao, and X. Y. Dong, "Highly sensitive fiber loop ringdown strain sensor using photonic crystal fiber interferometer," *Appl. Optics* **50**, 3087-3092 (2011).
7. L. M. Hu, C. C. Chan, X. Y. Dong, Y. P. Wang, P. Zu, W. C. Wong, W. W. Qian, and T. Li, "Photonic Crystal Fiber Strain Sensor Based on Modified Mach-Zehnder Interferometer," *IEEE Photon. J.* **4**, 114-118 (2012).
8. C. L. Zhao, L. M. Xiao, J. Ju, M. S. Demokan, and W. Jin, "Strain and temperature characteristics of a long-period grating written in a photonic crystal fiber and its application as a temperature-insensitive strain sensor," *J. Lightw. Technol.* **26**, 220-227 (2008).
9. L. Rindorf and O. Bang, "Highly sensitive refractometer with a photonic-crystal-fiber long-period grating," *Opt. Lett.* **33**, 563-565 (2008).

10. Y. Zhu, Z. He, and H. Du, "Detection of external refractive index change with high sensitivity using long-period gratings in photonic crystal fiber," *Sens. Actuators, B* **131**, 265-269 (2008).
11. J. Ju and W. Jin, "Photonic Crystal Fiber Sensors for Strain and Temperature Measurement," *J. Sensor* **2009**, 1-10 (2009).
12. J. Ju and W. Jin, "Long period gratings in photonic crystal fibers," *Photonic Sensors* **2**, 65-70 (2012).
13. V. P. Minkovich, J. Villatoro, D. Monzon-Hernandez, S. Calixto, A. B. Sotsky, and L. I. Sotskaya, "Holey fiber tapers with resonance transmission for high-resolution refractive index sensing," *Opt. Express* **13**, 7609-7614 (2005).
14. D. Monzon-Hernandez, V. P. Minkovich, J. Villatoro, M. P. Kreuzer, and G. Badenes, "Photonic crystal fiber microtaper supporting two selective higher-order modes with high sensitivity to gas molecules," *Appl. Phys. Lett.* **93**, 081106 (2008).
15. D. K. C. Wu, B. T. Kuhlmeier, and B. J. Eggleton, "Ultrasensitive photonic crystal fiber refractive index sensor," *Opt. Lett.* **34**, 322-324 (2009).
16. J. Mathew, Y. Semenova, and G. Farrell, "Photonic Crystal Fiber Interferometer for Dew Detection," *J. Lightw. Technol.* **30**, 1150-1155 (2012).
17. C. Wu, B. O. Guan, C. Lu, and H. Y. Tam, "Salinity sensor based on polyimide-coated photonic crystal fiber," *Opt. Express* **19**, 20003-20008 (2011).
18. M. Smietana, D. Brabant, W. J. Bock, P. Mikulic, and T. Eftimov, "Refractive-index sensing with inline core-cladding intermodal interferometer based on silicon nitride nano-coated photonic crystal fiber," *J. Lightw. Technol.* **30**, 1185-1189 (2012).
19. W. C. Wong, C. C. Chan, L. H. Chen, T. Li, K. X. Lee, and K. C. Leong, "Polyvinyl alcohol coated photonic crystal optical fiber sensor for humidity measurement," *Sens. Actuators, B* **174**, 563-569 (2012).
20. Z. Q. Tou, C. C. Chan, W. C. Wong, and L. H. Chen, "Fiber optic refractometer based on cladding excitation of localized surface plasmon resonance," *IEEE Photon. Technol. Lett.* **25**, 556-559 (2013).
21. T. Li, X. Y. Dong, C. C. Chan, K. Ni, S. Q. Zhang, and P. P. Shum, "Humidity sensor with a PVA-coated photonic crystal fiber interferometer," *IEEE Sensors J.* **13**, 2214-2216 (2013).
22. Y. C. Tan, Z. Q. Tou, V. Mamidala, K. K. Chow, and C. C. Chan, "Carbon-nanotube-deposited photonic crystal fiber for refractive index sensing," *Proc.SPIE-OFS23*, 91577Y-91577Y-4 (2014).
23. Y. C. Tan, Z. Q. Tou, V. Mamidala, K. K. Chow, and C. C. Chan, "Continuous refractive index sensing based on carbon-nanotube-deposited photonic crystal fibers," *Sens. Actuators, B* **202**, 1097-1102 (2014).
24. F. Yavari, N. Koratkar, "Graphene-based chemical sensors," *J. Phys. Chem. Lett.* **3**, 1746-1753 (2012).
25. J. Ma, W. Jin, H. F. Xuan, C. Wang and H. L. Ho, "Fiber-optic ferrule-top nanomechanical resonator with multilayer graphene film," *Opt. Lett.* **39**, 4769-4772 (2014).
26. J. N. Dash and R. Jha, "Graphene-based birefringent photonic crystal fiber sensor using surface plasmon resonance," *IEEE Photon. Technol. Lett.* **26**, 1092-1095 (2014).
27. B. C. Yao, Y. Wu, Y. Cheng, A. Q. Zhang, Y. Gong, Y. J. Rao, Z. G. Wang and Y. F. Chen, "All-optical Mach-Zehnder interferometric NH₃ gas sensor based on graphene/microfiber hybrid waveguide," *Sens. Actuators, B* **194**, 142-148 (2014).
28. Y. Wu, B. C. Yao, A. Q. Zhang, Y. J. Rao, Z. G. Wang, Y. Cheng, Y. Gong, W. L. Zhang, Y. F. Chen and K. S. Chiang, "Graphene-coated microfiber Bragg grating for high-sensitivity gas sensing," *Opt. Lett.* **39**, 1235-1237 (2014).
29. Y. Wu, B. C. Yao, A. Q. Zhang, X. L. Cao, Z. G. Wang, Y. J. Rao, Y. Gong, W. Zhang, Y. F. Chen and K. S. Chiang, "Graphene-based D-shaped fiber multicore mode interferometer for chemical gas sensing," *Opt. Lett.* **39**, 6030-6033 (2014).
30. M. Batumalay, S. W. Harun, F. Ahmad, R. Md Nor, N. R. Zulkepley, and H. Ahmad, "Tapered plastic optical fiber coated with graphene for uric acid detection," *IEEE Sensors J.* **14**, 1704-1709 (2014).
31. Y. C. Tan, W. B. Ji, V. Mamidala, K. K. Chow, and S. C. Tjin, "Carbon-nanotube-deposited long period fiber grating for continuous refractive index sensor applications," *Sens. Actuators, B* **196**, 260-264 (2014).
32. H. S. Skulason, P. E. Gaskell, and T. Szkopek, "Optical reflection and transmission properties of exfoliated graphite from a graphene monolayer to several hundred graphene layers," *Nanotechnology* **21**, 295709 (2010).
33. H. A. Macleod, *Thin-film Optical Filters, 4th ed.* (CRC/Taylor & Francis, 2010).
34. G. P. Keeley, A. O'Neill, N. McEvoy, N. Peltekis, J. N. Coleman and G. S. Duesberg, "Electrochemical ascorbic acid sensor based on DMF-exfoliated graphene," *J. Mater. Chem.* **20**, 7864-7869 (2010).
35. A. C. Ferrari, J. C. Meyer, V. Scardaci, C. Casiraghi, M. Lazzeri, F. Mauri, S. Piscanec, D. Jiang, K. S. Novoselov, S. Roth and A. K. Geim, "Raman spectrum of graphene and graphene layers," *Phys. Rev. Lett.* **97**, 187401 (2006).
36. S. F. O. Silva, O. Frazão, P. Caldas, J. L. Santos, F. M. Araújo and L. A. Ferreira, "Optical fiber refractometer based on a Fabry-Pérot interferometer," *Opt. Eng.* **47**, 054403 (2008).
37. Y. P. Miao, B. Liu, and Q. D. Zhao, "Refractive index sensor based on measuring the transmission power of tilted fiber Bragg grating," *Opt. Fiber Technol.* **15**, 233-236, (2009).

38. M. Jiang, Q. Li, J. Wang, W. Yao, Z. Jin, Q. Sui, J. Shi, F. Zhang, L. Kia and W. Dong, "Optical response of fiber-optic Fabry-Perot refractive-index tip sensor coated with polyelectrolyte multilayer ultra-thin films," *J. Lightw. Technol.* **31**, 2321-2326 (2013).
 39. S. Pevec and D. Donlagic, "Miniature fiber-optic sensor for simultaneous measurement of pressure and refractive index," *Opt. Lett.* **39**, 6221-6224 (2014).
 40. J. Villatoro, V. Finazzi, V. P. Minkovich, V. Pruneri, and G. Badenes, "Temperature-insensitive photonic crystal fiber interferometer for absolute strain sensing," *Appl. Phys. Lett.* **91**, 091109 (2007).
-

1. Introduction

Many studies into utilizing specialty fibers as sensing elements have been conducted over the years, resulting in highly sensitive sensors to perturbations in the refractive index (RI), strain and temperature of the external environment of the sensing elements. Of these, the more commonly used specialty fiber is that of the photonic crystal fiber (PCF). Many of these sensing elements involve the use of PCFs in an interferometric configuration [1-7], inscription of long period fiber gratings (LPGs) into PCFs [8-12], tapering the PCFs [13, 14] or filling the microstructure defects in the PCF with the analyte to be measured [15, 16]. In recent years, new types of sensing elements involving the deposition of specific materials to form thin overlays over specialty fibers for sensitivity enhancement have been proposed [17-23]. The choice of material for the overlays, apart from being compatible with silica fibers, would also depend on the material's ability to respond to the analyte being measured [17-19, 21] and/or its ability to further enhance the sensing capabilities of the particular sensing element [20, 22, 23]. The typical sensing schemes for these sensors would usually involve the monitoring of variations in wavelength or intensity level of the output spectral pattern in response to the aforementioned perturbations in the external environment.

More recently, it has been suggested that carbon-based compounds would be a good choice of material due to its relative ease of manipulability. Also, an optical fiber sensor with a carbon-based overlay to enhance its sensing capabilities would, from an industrial perspective, be more attractive in terms of its cost effectiveness and scalability [24]. This coupled with its unique properties have led to the development of several carbon-based fiber sensors [25-30]. Recently, we have proposed and investigated some specialty fiber sensors deposited with carbon nanomaterials [22, 23, 31] and in this paper, we present a pilot demonstration of an optical fiber RI sensor with a graphene overlay deposited over a bare PCF sensing element for continuous RI sensing. The graphene were deposited onto the bare PCF through a simple cold transfer method and did not require any additional physical or chemical treatment. It was found that the graphene had large surface areas which allowed them to adhere strongly to the PCF. The high RI of the resulting overlay altered the effective RI of the fiber cladding and consequently, the reflectance of the evanescent waves of the excited higher order cladding modes in the PCF segment. Hence, the graphene overlay modified the conventional sensing scheme of the sensor to that of variations in intensity as the RI of the external environment varied, which consequently allowed it to measure a wide range of RIs without the need for any reference measurements or limitations from its free spectral range (FSR). The sensor also demonstrated good repeatability and exhibited continuous measurement of RI with sensitivities of 9.4 dB/RIU and 17.5 dB/RIU for the RI ranges of 1.33-1.38 and 1.38-1.43, respectively.

2. Sensing principle

In this work, the sensing principle relies mainly on the behavior of light propagating through a PCF in a Mach-Zehnder Interferometer (MZI) configuration as well as the graphene overlay deposited onto the bare PCF segment in the MZI. A schematic of the conventional PCF MZI made from the splicing of a SMF to each end of a short segment of a PCF is shown in Fig. 1(a). As the fundamental mode from the SMF (solid line) enters the first collapsed region, it would be diffracted and excite some of the higher order cladding modes (dashed

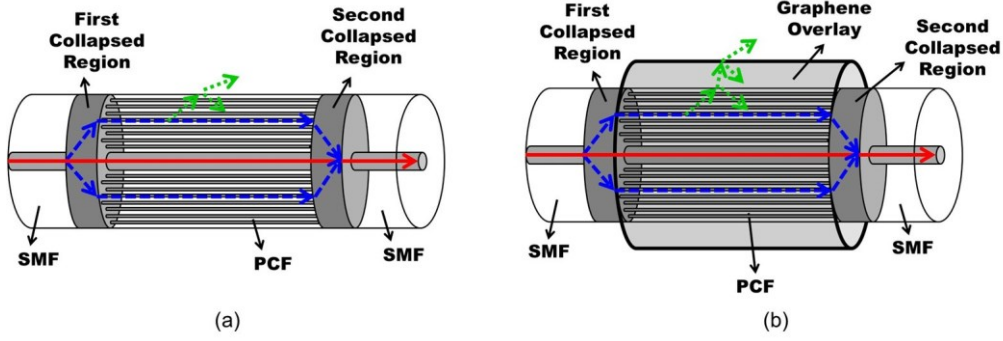


Fig. 1. Schematic illustration of the (a) photonic crystal fiber (PCF) spliced between two single mode fibers (SMFs) to form a PCF Mach-Zehnder Interferometer (MZI) and (b) the refractive index (RI) sensing element formed by the deposition of a graphene overlay onto the PCF segment.

line). These excited cladding modes would propagate along the cladding of the PCF and interfere and recombine with the fundamental mode at the second collapsed region. The intensity of the transmitted light monitored through the output SMF can thus be expressed as [2, 7]:

$$\begin{aligned}
 I_{total} = & E_{core}^2 + \sum_{i=1}^N E_{clad,i}^2 + 2 \sum_{i=1}^N [(E_{core} E_{clad,i})^{1/2} \cos \frac{2\pi (n_{core} - n_{clad,i})L}{\lambda}] \\
 & + 2 \sum_{i=1}^{N-1} \sum_{j=i+1}^N [(E_{clad,i} E_{clad,j})^{1/2} \cos \frac{2\pi (n_{clad,i} - n_{clad,j})L}{\lambda}]
 \end{aligned} \quad (1)$$

where E_{core} is the magnitude of the electric field of the core mode, while $E_{clad,i}$ and $E_{clad,j}$ are the magnitudes of the electric fields of the excited i^{th} and j^{th} order cladding modes, respectively. N is the total number of excited cladding modes. n_{core} is the effective RI of the core mode while that of the i^{th} and j^{th} order cladding modes are represented by $n_{clad,i}$ and $n_{clad,j}$, respectively. The length of the PCF segment in the MZI is denoted by L while λ represents the wavelength of light coupled into the MZI. As can be seen from Fig. 1(a), the evanescent waves of the cladding modes (dotted line) would be able to interact with the external environment. Due to this interaction with the external environment, $n_{clad,i}$ and $n_{clad,j}$ would vary with a variation in RI of the external environment. Hence it can be seen from Eq. (1), and also previously experimentally verified in [1], that a variation in RI of the external environment would result in a blue or red shift of the interference peaks or dips in the output spectrum.

Fig. 1(b) shows a schematic of the PCF segment of the MZI with the deposited graphene overlay. The deposition of graphene onto the bare PCF segment would result in the modification of the sensing scheme of the sensing element. Graphene, like other carbon nanomaterials, are a carbon nanomaterial which also has a high RI and exhibits unique optical properties [32]. From Eq. (1), it can be seen that the high RI of the graphene would increase the effective index of the fiber cladding and due to this increase, a variation in RI of the external environment would lead to minimal variations in the cosine terms. Hence, little variation in the wavelength of the interference peaks or dips in the output spectrum would be expected. The evanescent waves of the excited cladding modes would, on the other hand, experience a variation in reflectance which would result in a variation in the extinction ratio observable in the output spectrum and this reflectance can be expressed as [33]:

$$R = \left| \frac{r_{23} + r_{34} e^{-i\tilde{k}_G}}{1 + r_{23} r_{34} e^{-i\tilde{k}_G}} \right|^2 \quad (2)$$

where

$$r_{2,3} = \frac{n_{clad} - \tilde{n}_G}{n_{clad} + \tilde{n}_G} \quad (3)$$

$$r_{3,4} = \frac{\tilde{n}_G - n_{env}}{\tilde{n}_G + n_{env}} \quad (4)$$

$$\tilde{k}_G = \frac{4\pi\tilde{n}_G d_G}{\lambda} = \frac{4\pi n d_G}{\lambda} - i \frac{4\pi k d_G}{\lambda} = \beta_G - i a d_G \quad (5)$$

where $r_{2,3}$ and $r_{3,4}$ represent the amplitude reflection coefficients of the interface between the fiber cladding and the graphene overlay and the interface between the graphene overlay and the external environment, respectively. $a = 4\pi k / \lambda$ and d_G are the absorption coefficients and the thickness of the graphene overlay, respectively. The RIs of the graphene, fiber cladding and that of the external environment are denoted by \tilde{n}_G , n_{clad} and n_{env} , respectively. It can be seen from Eqs. (2) to (5) that the reflectance R is dependent on the RI of the external environment n_{env} . This would indicate that as the RI of the external environment varied, so would the intensities of the evanescent waves of the excited cladding modes, leading to a variation in the intensities of the excited cladding modes, and thus cause a variation in amplitude of any interference peaks or dips present in the output spectrum.

3. Fabrication of sensing element

Fig. 2(a) shows the experimental setup used for the fabrication of the proposed sensing element. A PCF (NKT photonics LMA-10) was first stripped off its polymer coating and spliced between two SMFs to form a MZI. The length of the PCF segment was measured to be 30 mm. A graphene solution was prepared by mixing Kish Graphite (Graphene Laboratories Inc.) with dimethylformamide (DMF) [34]. The resulting solution was then sonicated in an ultrasonic water bath to ensure that the graphene were separated and evenly dispersed throughout the solution.

A broadband light source (Optical Link Limited CL 15-16 ASE) with a wavelength range of 1510-1630 nm was coupled into the SMF at one end of the MZI. At the other end, the transmitted light was coupled into an Optical Spectrum Analyzer (OSA, Ando AQ6317B) and monitored with a resolution of 0.1 nm as shown in Fig. 2(a). To fabricate the sensing element

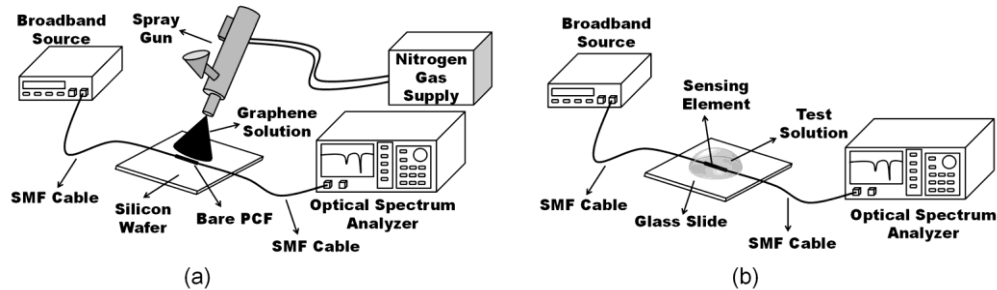


Fig. 2. Experimental setups for (a) the deposition of the graphene overlay onto the PCF segment using a spray gun and (b) for RI measurements with various test solutions of different RIs.

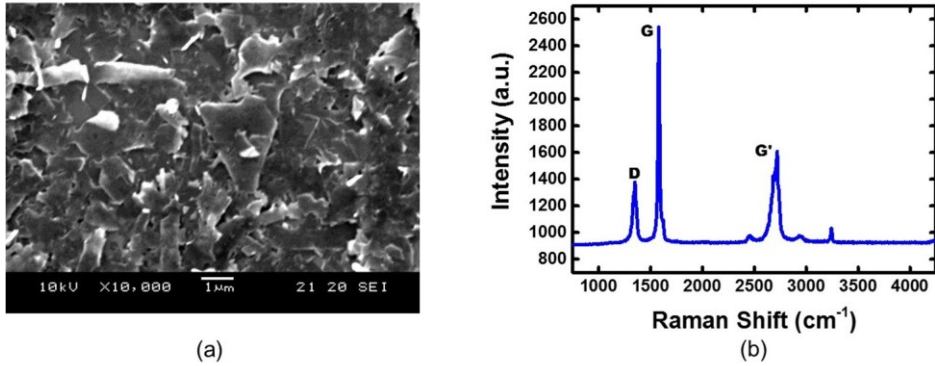


Fig. 3. (a) Raman spectra of the graphene solution and (b) Scanning electron microscope (SEM) image of the graphene deposited on a silicon wafer.

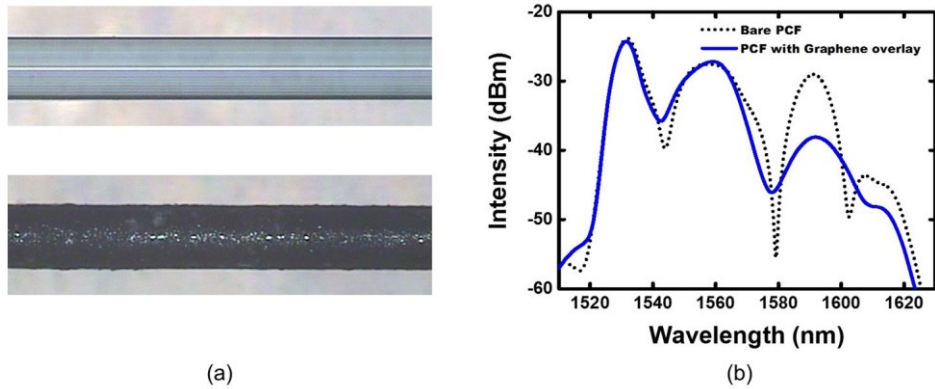


Fig. 4. Optical microscope images of the PCF segment before (above) and after (below) the deposition of the graphene overlay under the same magnification and (b) output spectrum before (dotted line) and after (solid line) the deposition of the graphene overlay.

shown in Fig. 1(b), the PCF segment was held straight over a silicon wafer. A portion of the graphene solution was then extracted into the solution cup of a spray gun (Harder and Steenbeck, Evolution Two in One), which was connected to a nitrogen gas supply, and deposited for a duration of 1 s over the bare PCF segment and silicon wafer at the same time. The PCF segment was then rotated 90 degrees after the first deposition and deposited with graphene over the same spray duration. The process was repeated two more times to ensure that graphene was evenly deposited over the entire PCF. The adherence of the graphene onto the PCF depends only on the van der Waal's forces between the graphene overlay and the PCF segment. The resulting output spectrum was monitored throughout the deposition process to ensure that an interference spectrum with interference dips of sufficiently high extinction ratio were still present. The Raman spectra of the graphene deposited on the silicon wafer is shown in Fig. 3 (a). The presence of the D, G and G' bands at 1349 cm⁻¹, 1578 cm⁻¹ and 2719 cm⁻¹ show that the graphene are similar to that of bulk graphite or multilayer graphene [35]. The presence of the D band is to be expected due to defects in the graphene during the sonication process. The morphology of the deposited graphene on the silicon wafer was then observed by a scanning electron microscope (SEM) as shown in Fig. 3(b). It is observed that graphene are evenly and randomly deposited over the

wafer and this can be assumed to be the case for the deposited graphene on the PCF segment as well. Similarly, the thickness of the graphene deposited onto the silicon wafer was measured by a surface profiler (Dektak³) and from there the thickness of the graphene deposited onto the PCF segment was calculated to be approximately 40 nm. Fig. 4(a) shows the optical microscope images of the PCF segment before (above) and after (below) the deposition of the graphene overlay. As can be observed, the entire surface of the PCF was considerably darkened by the graphene, and the graphene were evenly deposited over the PCF. The output spectrum (monitored by the OSA) before and after the deposition of the graphene overlay is shown in Fig. 4(b). For sensing purposes, the interference dip at a wavelength of 1579.24 nm before deposition (dotted line) was chosen. The choice of this interference dip is due to its high extinction ratio, its close proximity to the telecommunications wavelength of 1550 nm, and that this interference dip would be the result of interference with a higher order mode and thus be more sensitive to changes in the RI of the external environment. As can be seen, there was a blue shift of the interference dip to a wavelength of 1577.68 nm with an approximately 9 dB decrease in magnitude after the deposition (solid line) of the graphene overlay. The exact cause of this effect is still unknown and is currently under investigation. As the deposition only involves the cold transfer of graphene onto the surface of the PCF without any additional physical or chemical treatment, such a deposition technique will be relatively cost effective compared to other deposition methods.

4. Experiment and discussion of results

Fig. 2(b) shows the experimental setup used for RI measurements. Solutions of different RI values were prepared by first continuously dissolving sugar in a fixed volume of de-ionized (DI) water to obtain a saturated sucrose solution. The saturated solution was then divided equally into smaller portions and each portion was diluted with a different amount of DI water to obtain sucrose solutions of different concentrations and hence different RIs. A commercially available digital refractometer (Kruss DR201-95) with a resolution of 0.0001 refractive index units (RIUs) was used to measure the RI of each solution. To characterize the behavior of the sensor to different RIs, the sensing element was held straight over a rectangular glass slide and completely immersed in approximately 1 ml of the individual sucrose solutions which were dropped over the glass slide. The same broadband light source and OSA, as mentioned in the previous section, were used to couple light into the sensing element and monitor the output spectrum, respectively. The glass slide and the sensing element were rinsed thoroughly with DI water and left to dry after each RI measurement was

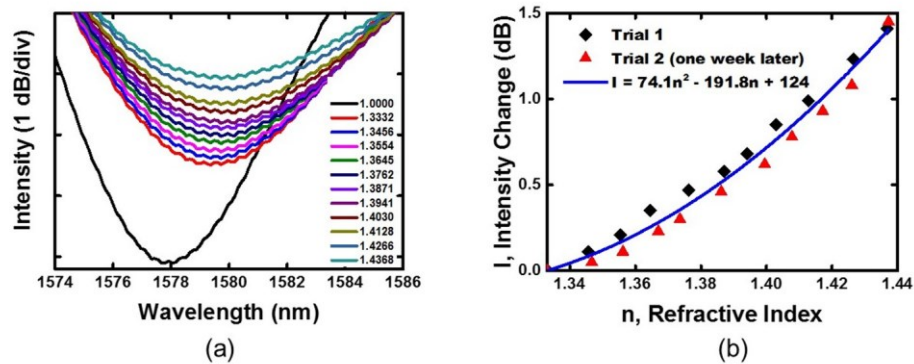


Fig. 5. (a) Output spectra of the sensing element, focusing particularly on the variation of the selected interference dip at 1577.68 nm when the sensing element was immersed in various solutions of different RIs. (b) Plot of the change in intensity of the interference dip shown in (a) against the RI of the various solutions for two separate trials (diamonds and triangles) conducted one week apart. The nonlinear behavior of the sensing element to variations in RI is illustrated by the single fitting curve (solid line).

carried out. It was ensured that the spectral pattern for the sensing element in air, as shown in Fig. 4(b) (solid line), was recovered before the next measurement was carried out. The entire trial was carried out at an ambient temperature of 22.8 ± 0.1 °C to ensure that there were no temperature induced perturbations in the external environment which would affect the RI measurements in any way.

Fig. 5(a) shows the output spectrum of the sensing element when it was immersed in various solutions of different RI, focusing in particular on the selected interference dip at 1577.68 nm. As can be seen, distinguishable variations in the amount of attenuation of the interference dip can be observed as the RI of the external environment varied. The magnitude of the intensity of the interference dip decreased as the RI of the external environment increased. On the other hand, there was little observable variation in the wavelength of the monitored interference dip. The observed behavior of the intensity and wavelength of the interference dip is consistent with that of Eqs. (1) to (5) where, for this range of RIs, the amount of reflectance would decrease due to the increasing RI of the external environment. Hence, a portion of the energy of the evanescent waves is coupled out of the excited cladding modes near the external surface of the fiber cladding, resulting in an observable decrease in the magnitude of the interference dip in the output spectra. The high RI of the graphene overlay would increase the effective index of the cladding, leading to minimal variations in the cosine terms in Eq. (1) as the RI of the external environment varies. This would result in little variation in the wavelengths of the interference peaks and dips in the output spectrum, which has been experimentally verified from the results shown in Fig. 5(a). The experiment was repeated a week later, under similar experimental conditions and procedures as that described above, to test the repeatability of the sensing element. A similar result was obtained and the variation in magnitude of the intensities of the interference dips to various RIs from both trials for the sensing element is shown in Fig. 5(b). For each trial, the difference in intensity of the interference dip at each RI value was plotted relative to the intensity value of the point corresponding to the lowest RI value for that trial. A single fitting curve (solid line) was then plotted through the data points (diamonds for the first trial and triangles for the second trial) for the two trials. From there, the maximum error due to the repeatability of the sensing element can be calculated to be 0.1 dB. This error can be attributed to fluctuations in the output power of the broadband source as well as measurement errors from the OSA. As can be seen from Fig. 5(b), there is a nonlinear relationship between the intensity of the interference dip and the RI, which is consistent with Eqs. (2) to (5). The results show that the sensor demonstrates good repeatability and also exhibits consistency in its behavior with respect to variations in RI of the external environment. Based on the obtained results, the sensing element was able to achieve a sensitivity of 9.4 dB/RIU and 17.5 dB/RIU for the RIs of 1.33-1.38 and 1.38-1.43, respectively. From here, the maximum resolution can be calculated to be approximately 5×10^{-4} which an order of magnitude above that of refractometers based on a fiber Bragg grating [36] and a tilted fiber Bragg grating [37]. On the other hand, it is not as sensitive as some of the other reported fiber sensors that use surface plasmon resonance [20, 26] or precision fabrication of a Fabry-Pérot cavity in the sensing element [38, 39]. However, the current sensor has certain advantages in that it does not show any signs of degradation in performance as compared to that in [20], and also in its relative fabrication simplicity as compared to that of [26, 38, 39].

It should be pointed out that as the sensing scheme was modified, the sensor was not limited by its FSR. Hence there was no need for any reference measurements to be taken during the experimental process as it was possible for the sensing element to measure a wide range of RIs (1.0 to 1.43) continuously. Also, as can be seen from Eqs. (2) to (5), the amount of reflectance from the graphene overlay depends mostly on the RI of the external environment and is minimally affected by other factors like strain and temperature. Hence, the behavior of the sensing element to perturbations like temperature and strain would be expected to be similar to that described in [40]. It would then be possible to measure a second

perturbation to the sensor, like strain for example, simultaneously through variations in wavelength in the output spectrum, and thus enhance the sensor's potential as a dual parameter sensor. As the current work serves only as a pilot demonstration of a graphene-deposited PCF sensing element, a further exploration into methods for enhancing the sensitivity and the reproducibility of the sensing element would be carried out. Future work will also focus on the effects of the morphology of the graphene overlay, as well as the influence of polarization and pH and the robustness of the graphene overlay under different environmental stresses. Also, as RI measurement of the external environment depends on the change in intensity in the output spectrum, fluctuations in the output of the broadband source would result in errors in the measurements. Hence possible ways to overcome these fluctuations, including modifying the experimental setup to include a reference arm to offset these errors, will be explored as part of the future work as well.

5. Conclusion

In conclusion, we have presented a pilot demonstration of a refractive index (RI) sensor based on the deposition of a graphene overlay onto the surface of a photonic crystal fiber (PCF) segment in a Mach-Zehnder Interferometer (MZI) configuration. The sensing element was fabricated through the fusion splicing of a single mode fiber (SMF) to each end of a short segment of a photonic crystal fiber (PCF) and thereafter depositing graphene onto the bare PCF segment using a spray gun. The high RI of the graphene overlay modified the sensing scheme of the MZI RI sensor allowing for continuous RI measurements and also brings to light the possibility for further studies into dual parameter sensing, where a second parameter which would cause a variation in the wavelength of the spectral peaks or dips can be characterized. Apart from that, the modification also allowed the sensor to overcome any limitations in its detectable range arising from its free spectral range. The sensor was also able to display observable and resolvable variations in the intensity of the selected interference dips as the RI of the external environment varied and has also demonstrated good repeatability with regards to its sensing behavior. Overall, the achieved sensitivity of the fabricated sensor was 9.4 dB/RIU for the RIs of 1.33-1.38 and 17.5 dB/RIU for the RIs of 1.38-1.43.

Acknowledgements

This work was partially supported by Academic Research Fund Tier 2 Grant (ARC26/14) of Ministry of Education (MOE), Singapore.